

Adaptive probabilistic shaped modulation for high-capacity free-space optical links

*Original*

Adaptive probabilistic shaped modulation for high-capacity free-space optical links / Guiomar, F. P.; Lorences-Riesgo, A.; Ranzal, D.; Rocco, F.; Sousa, A. N.; Fernandes, M. A.; Brandao, B. T.; Carena, A.; Teixeira, A. L.; Medeiros, M. C. R.; Monteiro, P. P.. - In: JOURNAL OF LIGHTWAVE TECHNOLOGY. - ISSN 0733-8724. - STAMPA. - 38:23(2020), pp. 6529-6541. [10.1109/JLT.2020.3012737]

*Availability:*

This version is available at: 11583/2902292 since: 2021-05-23T20:51:55Z

*Publisher:*

Institute of Electrical and Electronics Engineers Inc.

*Published*

DOI:10.1109/JLT.2020.3012737

*Terms of use:*

This article is made available under terms and conditions as specified in the corresponding bibliographic description in the repository








*Publisher copyright*

IEEE postprint/Author's Accepted Manuscript

©2020 IEEE. Personal use of this material is permitted. Permission from IEEE must be obtained for all other uses, in any current or future media, including reprinting/republishing this material for advertising or promotional purposes, creating new collecting works, for resale or lists, or reuse of any copyrighted component of this work in other works.

(Article begins on next page)

# Adaptive Probabilistic Shaped Modulation for High-Capacity Free-Space Optical Links

Fernando P. Guiomar , Abel Lorences-Riesgo , Daniel Ranzal, Federico Rocco, Artur N. Sousa, Marco A. Fernandes , Bruno T. Brandão , Andrea Carena , António L. Teixeira , Maria C. R. Medeiros, and Paulo P. Monteiro 

**Abstract**—Infrared free-space optics (FSO) provide an attractive solution for ultra-high-capacity wireless communications. However, the full potential of FSO is still being hindered by the apparent random fluctuations on the received optical power, which can be triggered by external factors such as atmospheric turbulence, weather instability and pointing errors. Through the analysis of long-term experimental measurements, we identify the existence of significant time-domain memory in outdoor FSO links, which is found to be particularly strong under rainy weather conditions. Following this observation, we demonstrate that these memory effects can be effectively utilized to design accurate FSO channel estimation algorithms. Taking advantage of the arbitrary bit-rate granularity provided by probabilistic constellation shaping (PCS), and resorting to a simple moving average channel estimator, we demonstrate 400G+ transmission over a seamless fiber-FSO 55 m link with enhanced resilience towards adverse weather conditions. Comparing with unsupervised fixed modulation, we demonstrate a significant increase in average bit-rate (>35 Gbps) after continuous measurement over 3 hours, including raining periods.

**Index Terms**—Free-space optics, probabilistic shaping, adaptive modulation.

## I. INTRODUCTION

THE proliferation of wireless communication services has been progressively leading to a strong spectrum congestion in the over-exploited sub-6 GHz band, with more than 6 billion mobile broadband subscriptions reported by the end of 2019 [1]. In order to face this challenge, the recently standardized 5G wireless communications [2] already include support to mm-wave transmission [3], whose carrier frequencies are typically within the range of 30 GHz

to 300 GHz. With the aim of supporting beyond 5G communications and its promised ultra-high bit-rates above 100 Gbps [4], several research efforts are already focusing on the usage of THz-wave radiation [5], thereby extending wireless communications into the band of 300 GHz to 3 THz. However, in contrast with the legacy sub-6 GHz band, both mm-wave and THz-wave essentially require line-of-sight (LOS) communication [6], thus bringing a key paradigm change in terms of wireless signal propagation. Another very limiting aspect is the enormous cost increase of the radio-frequency (RF) components (mixers, amplifiers, filters, ...) that are required for transmission at such high frequencies and bandwidths. Actually, these technical limitations are clearly reflected by the limited reach that has been demonstrated so far with THz-wave links [7]–[9]. A couple of notable exceptions can be found in [10], [11], where transmission over 100 m indoor links has been demonstrated for 50–100 Gbps signals at a carrier frequency of 300 GHz.

Taking advantage of this paradigm shift towards LOS wireless communications, the use of free-space optics (FSO) in the near-infrared (NIR) region [12] has recently been attracting a strong interest for high-speed wireless communications, providing a higher-capacity and lower-cost alternative to THz-wave transmission. Benefiting from the eye-safety operation and low atmospheric attenuation within the 1550 nm window (unlicensed spectrum) [13], standard low-cost photonic components that are typically used for fiber-based communications can also be utilized for signal transmission via FSO [14]. Current FSO application scenarios span from indoor [15] to inter-satellite communications [16], being also considered as a wireless alternative to fiber-based transmission in terrestrial links [17], [18], providing a rapid recovery solution in disaster scenarios. In addition, following several recent research works, FSO is also becoming a promising candidate for ultra-high capacity fronthauling in 5G and beyond access networks [19], [20].

Despite its tremendous potential for ultra-high-speed point-to-point wireless communications, the impact of atmospheric turbulence and various weather phenomena are still critical aspects for outdoor FSO communications [21]–[23]. Driven by changes of temperature and pressure in the atmosphere, atmospheric turbulence gives rise to sudden variations on the refractive index of the air along the transmission path, which results in the phenomenon of optical scintillation: a turbulence-induced time-dependent optical power fading [24]. In addition, in seamless fiber-FSO systems, where the

This work was partially supported by the European Regional Development Fund (FEDER), through the Regional Operational Programme of Centre (CENTRO 2020) of the Portugal 2020 framework, through projects ORCIP (CENTRO-01-0145-FEDER-022141), SOCA (CENTRO-01-0145-FEDER-000010) and RETIOT (POCI-01-0145-FEDER-016432), and by FCT/MCTES through project FreeComm-B5G (UIDB/EEA/50008/2020).

Fernando P. Guiomar, Daniel Ranzal, Artur N. Sousa, Marco A. Fernandes, Bruno T. Brandão, António L. Teixeira and Paulo P. Monteiro are with Instituto de Telecomunicações, University of Aveiro, 3810-193, Aveiro, Portugal (e-mail: guiomar@av.it.pt)

A. Lorences-Riesgo was with Instituto de Telecomunicações, 3810-193, Aveiro. He is now with Huawei Technologies France, 92100 Boulogne-Billancourt, France.

Federico Rocco and Andrea Carena are with Dipartimento di Elettronica e Telecomunicazioni, Politecnico di Torino, Corso Duca degli Abruzzi, 24, 10129 Torino, Italy (e-mail: andrea.carena@polito.it).

Maria C. R. Medeiros is with Instituto de Telecomunicações, Universidade de Coimbra, 3030-290, Coimbra, Portugal (email: cmedeiros@deec.uc.pt)

Manuscript received March XX, 2020; revised April XX, 2020.

optical signal is directly coupled to the fiber core typically using fiber collimators, the system performance can also be strongly affected by changes in the angle-of-arrival of the received optical beam [21]. As a consequence of these effects, the effective signal-to-noise ratio (SNR) experienced by the FSO receiver may suffer from large variations, resulting in a drastic reduction of the communication reliability. In order to characterize these optical amplitude fluctuations, several statistical models have been proposed in the literature, among which the log-normal [25] and gamma-gamma [26] distributions have attracted considerable attention. Nevertheless, besides the stochastic distribution of optical power fading, it is also critical to analyze both the coherence bandwidth (i.e. the correlation between different frequencies that may lead to pulse broadening) and the coherence time (i.e. the correlation between different time instants) [27] in outdoor FSO links. In this particular aspect, FSO systems are known to be heavily penalized by fog [28], in which case the coherence bandwidth of the system can be in the order of a few MHz [29], thus introducing a strong pulse distortion along the propagation. Nevertheless, it has been numerically and experimentally demonstrated that FSO systems are relatively robust to the impact of rain [28]–[30], which typically implies coherence bandwidths above 100 GHz [29]. The same applies to the standalone impact of atmospheric turbulence, whose coherence bandwidth is typically in the THz range, even in the strong turbulence regime [29]. Therefore, except for the particularly challenging fog scenario, an FSO system can be generally characterized by a frequency-flat response [31], which makes it notably adequate for single-carrier modulation schemes. In turn, the coherence time of atmospheric turbulence is typically within the range of  $10\ \mu\text{s}$  –  $10\ \text{ms}$  [28], while significantly longer coherence times of few seconds up to several minutes can arise from large-scale atmospheric turbulence events and other weather-related phenomena [32], such as slow changes of temperature and rainfall intensity. Therefore, for typical symbol-rates in the Gbaud range, FSO systems can be accurately described by a block-fading model [33], which opens up the opportunity for the implementation of various time-adaptive transmission schemes, including transmitter power control [34]–[38], adaptive modulation [35]–[37], adaptive coding [36]–[39], automatic repeat request protocols, spatial and/or time diversity [40]–[44], maximum likelihood sequence detection [45], [46] and hybrid RF-FSO transmission [47]–[49].

Due to its simplicity and low-cost, commercial FSO communications typically rely on on-off keying (OOK) modulation and direct detection [50]. However, this kind of signal modulation and detection provides only one degree of freedom (amplitude) for encoding the transmitted information, thereby strongly limiting the achievable channel capacity. After a decade of intensive developments, multi-level quadrature-amplitude modulation (QAM) together with coherent detection has achieved maturity in fiber-optic communication systems [51]. Targeting a further improvement of communication efficiency, probabilistic constellation shaping (PCS) has recently been proposed for optical

communications systems [52], finding a rapid dissemination of both research and commercial applications [53], [54]. As opposed to standard QAM constellations, which are typically composed of independent and identically distributed (i.i.d.) symbols, the concept of PCS lies on the assignment of a given probability distribution function to its constellation symbols, thereby controlling both the entropy and average transmitted signal energy. When the Maxwell-Boltzman distribution is applied to set the probability of appearance of each constellation symbol in additive white Gaussian noise (AWGN) channels, it has been shown that PCS can provide a reduction of transmitted power by up to 1.53 dB [55]. This effect is commonly referred in the literature as the PCS shaping gain, and it has been the main driver behind its rapid adoption in optical fiber systems. In addition, the recent development of implementable fixed-length distribution matchers [56] to set the PCS symbol probabilities, also provides another key advantage in terms of enhanced flexibility and granularity for controlling the transmitted net bit-rate [57]. This particular aspect can be highly advantageous for transmission systems with time-varying capacity, as it is the case of FSO communications.

Building upon the preliminary results published in [58], in this paper we exploit the modeling and mitigation of FSO transmission impairments in outdoor links, by resorting to long-term measurements under variable atmospheric conditions. Through the experimental analysis of optical power budget evolution over time in a 55 m outdoor FSO link, we develop a simple and accurate channel estimator, which can be used to track its time-varying SNR in real-time. Taking advantage of the bit-rate flexibility provided by PCS, we also experimentally demonstrate a time-adaptive modulation scheme, enabling to continuously adjust the transmission rate of a 400G+ FSO system over time, thereby improving the channel capacity and reliability.

The remainder of this paper is organized as follows. In Section II, we carry out an experimental modeling of power budget in outdoor FSO systems, providing the basis for the development of accurate channel monitoring tools. In Section III, we review the basics of PCS modulation, focusing on its potential and requirements for bit-rate adaptation. Bringing together the outcomes from the previous two sections, in Section IV we experimentally demonstrate a time-adaptive 400G+ transmission system over an outdoor 55 m FSO link impaired by intermittent rainy periods. Finally, the main conclusions from this work are summarized in Section V.

## II. POWER BUDGET MODELING OF OUTDOOR FSO LINKS

In this section, we aim at the modeling of power budget variations in an outdoor 55 m FSO link, resorting to long-term measurements of received optical power under variable meteorological conditions. All experimental results and respective post-processing routines presented in this section are made available for consulting in [59].

### A. Experimental Setup and Optical Power Measurements

The utilized experimental setup for FSO power budget measurement is depicted in Fig. 1. Assuming that the impact of

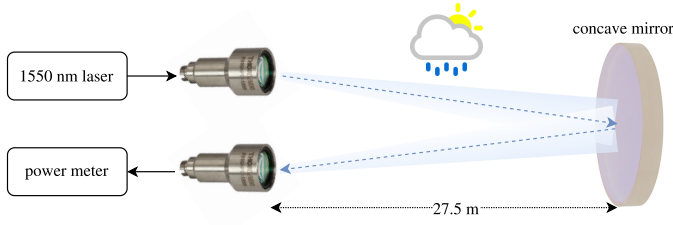


Fig. 1. Experimental setup of a seamless fiber-FSO outdoor link for optical power budget characterization.

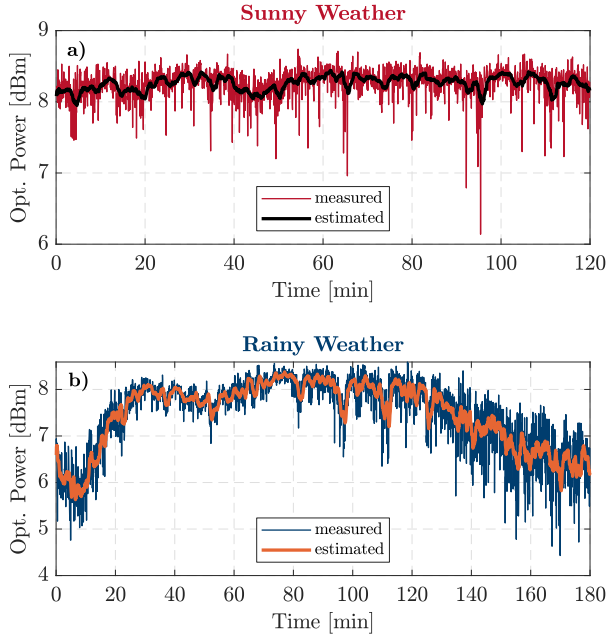


Fig. 2. Measured received optical power after 55m FSO transmission considering different meteorological conditions: a) sunny and b) rainy weather. The thick solid lines show the estimated optical power using a moving average with optimized memory depth (i.e. using  $N_{\text{taps,opt}}$  past measurements).

scintillation on the received optical power is mostly frequency-flat within the typical transmission bandwidths (tens of GHz), we consider a simplified experimental apparatus, in which the optical source consists of a continuous wave (CW) laser source operating at 1550 nm with 11 dBm output power. The seamless interface between fiber and free-space is performed by a pair of fiber collimators with 24 mm diameter, a divergence angle of  $0.0017^\circ$ , numerical aperture of 0.24 and focal length of 37.13 mm. At 27.5 m from the transmitter we place a concave mirror with  $\sim 30$  m focal length to reflect the optical signal back into the receiver, thus resulting in a total link length of 55 m. After the receiver fiber collimator, a power meter with a sampling rate of 0.25 Hz is utilized to continuously measure and register the received optical power. Although the relatively slow sampling-rate considered in this work effectively prevents the impact of spurious spatial correlation effects over the mirrored propagation path, it is worth referring that further experimental validation targeting higher update-rates should preferably avoid optical transmission over a folded propagation path.

In this paper, we will consider two different long-

term measurements obtained under distinct meteorological conditions:

- i) a 2-hour measurement during clear sky and dry sunny weather conditions;
- ii) a 3-hour measurement during a rainy day with sporadic rain showers.

The instantaneous measured received optical power for these two case studies are depicted in Fig. 2. As one would expect, the obtained results clearly show that the FSO link becomes much more unstable during rainy weather conditions: while the received optical power during sunny weather shows a standard deviation of roughly  $-5$  dBm, the corresponding standard deviation during rainy weather is increased to about  $-0.3$  dBm. In addition, the range of registered received optical powers (ratio between maximum and minimum powers) is increased from 2.6 dB to about 4.2 dB. The additional optical power loss and instability of the FSO link when affected by rain can be attributed to the scattering of light on the water droplets and to the refraction of the input and output light beams on the wet collimator lenses and mirror surface. Nevertheless, despite the additional loss, it is demonstrated that FSO transmission can effectively be considered during rainy weather conditions, provided that the corresponding power budget is taken into consideration.

For the reader that might be potentially interested in a more detailed analysis of the impact of rain and other weather phenomena on outdoor FSO power budget, it is worth referring to other research works currently available in the literature [21]–[23]. A notable example is the work of [21], in which the received optical power is directly correlated with the measured rain-rate in an outdoor link with 1 km distance between FSO transceivers. Instead of an in-depth modeling of these effects, within the scope of this paper we will focus our attention on the continuous tracking of received optical power, targeting the demonstration of a novel time-adaptive modulation technique.

### B. Time-Varying FSO Channel Monitoring

In order to enable the real-time monitoring of FSO power budget, an important observation that can be taken from Fig. 2 is that the measured FSO power seems to have some non-negligible time-domain correlation. To better characterize this apparent time-correlation, in Fig. 3a we depict the normalized autocovariance,  $K(t)$ , of the received optical power. Following the definition utilized in [28], we determine the channel coherence time by finding  $t$  such that  $K(t) = 1/e$ . Due to the increased time-variant nature of the unstable rainy weather scenario, the corresponding autocovariance function of the received optical power shows a much wider tail, with a coherence time of approximately 15 minutes. In contrast, the  $1/e$  coherence time associated with the sunny weather scenario is below the 4 s sampling period of the power meter. This provides further evidence that the optical power variations generated by atmospheric turbulence in ideal weather conditions exhibit a coherence time that is significantly shorter than the considered sampling period. Therefore, its effective tracking and compensation would require a faster optical power sampling. While this would

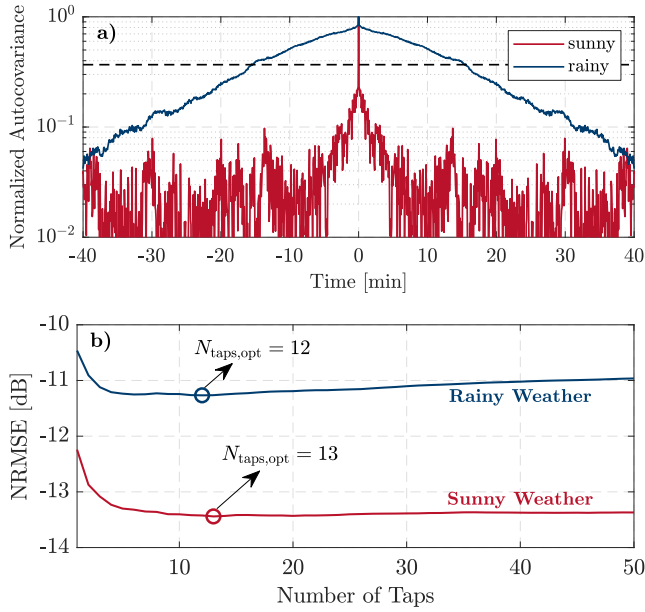


Fig. 3. a) Normalized autocovariance of the measured received optical power (the dashed line indicates the  $1/e$  threshold for coherence time evaluation) and b) memory depth optimization of the moving average power estimator under sunny and rainy weather conditions.

be possible with negligible added hardware complexity, its demonstration in an optical communications setup would require real-time processing, which is particularly challenging at the transmitted bit-rates considered in this work (400G+). Therefore, the main goal of this work is to demonstrate a proof-of-concept adaptive modulation scheme based on PCS modulation, which can be used to adapt the transmitted bit-rate according to the slow variations of received optical power caused by weather changes, which are more evident during raining periods. The identification of such time-domain memory effects can be utilized in favor of monitoring the evolving power budget of the FSO link. Although more complex options can be considered, for the sake of real-time feasibility, in this paper we propose the use of a simple unweighted  $N_{\text{taps}}$ -taps moving average optical power estimator,

$$P_{\text{est}}(n+1) = \frac{1}{N_{\text{taps}}} \sum_{n=N_{\text{taps}}+1}^n P_{\text{meas}}(n), \quad (1)$$

where  $P_{\text{meas}}(n)$  is the measured received optical power (in Watt) at time instant  $n$ , and  $P_{\text{est}}(n+1)$  is the estimated power for the next time instant. Making use of the recorded optical power measurements, we now simulate the task of channel estimation by applying the moving average estimator of expression (1) over the previous  $N_{\text{taps}}$  power measurements in order to estimate the next optical power. With the aim to optimize the memory depth of the moving average estimator, in Fig. 3b we show the normalized root-mean-square error (NRMSE) between the estimated and measured optical power, defined as

$$\text{NRMSE} = \frac{\sqrt{\frac{1}{N} \sum_{n=1}^N (P_{\text{est}} - P_{\text{meas}})^2}}{\frac{1}{N} \sum_{n=1}^N P_{\text{meas}}}, \quad (2)$$

where  $N$  is the total number of optical power measurement points.

The obtained results plotted in Fig. 3b indicate an optimum number of taps,  $N_{\text{taps,opt}}$ , of 12 and 13, for the cases of sunny and rainy weather, respectively. Considering the power meter sampling frequency of 0.25 Hz, this corresponds to approximately 50 s of memory depth for the moving average power estimator. The corresponding estimated optical power using the optimized  $N_{\text{taps,opt}}$  values is shown by the thick solid lines in Fig. 2, where we can see that the estimation effectively follows the average trend of the measurements, while it filters out the higher frequency components. Also note that, due to the quite stable performance of the FSO link during sunny weather conditions, the use of a larger number of taps only leads to a slight increase of the NRMSE. On the contrary, due to the quickly varying conditions associated with the rainy weather measurements, the use of longer memory depths on the moving average estimator leads to a progressive degradation of the estimation performance.

### C. Optimizing FSO Transmission Reliability

Ultra-high communication reliability is a key requirement for next-generation wireless transmission systems. In this sense, guaranteeing a high level of reliability in FSO systems becomes even more critical due to the inherent power budget fluctuations. In order to ensure reliable communication, we must consider a safety margin for operation, i.e. the channel capacity must be conservatively allocated so that any sudden drop of optical power budget does not bring the system below its error-free threshold. Assuming that the time-varying optical power budget can be estimated using the tools introduced in the previous subsection, then the FSO system can be adaptively loaded so that the error-free threshold follows the estimated received optical power. In order to account for inevitable errors during channel estimation, a given power budget margin,  $P_{\text{margin}}$ , should also be allocated. Otherwise, any slight overestimation of the optical power budget would bring the system into out-of-service state. In that case, the instantaneous communication reliability,  $R$ , will only be threatened whenever the difference between the estimated power and the actual measured power is larger than the operation margin,

$$R(n) = \begin{cases} 1, & P_{\text{est,dBm}}(n) - P_{\text{meas,dBm}}(n) \leq P_{\text{margin,dB}} \\ 0, & \text{otherwise.} \end{cases} \quad (3)$$

The long-term communication reliability can then be evaluated by taking the average value of  $R$  over all measurements,  $\bar{R}$ .

Using the definition of expression (3), in Fig. 4 we show the optimization of the FSO power margin for both meteorological scenarios. The estimated power,  $P_{\text{est,dBm}}$ , is obtained from the moving average power estimator of expression (1) with the optimized number of taps obtained from Fig. 3b. From the results of Fig. 4 we can clearly observe the impact of rain on the communication reliability of FSO communications. Indeed, while a power margin of  $\sim 1.3$  dB is enough to guarantee a reliability above 99.9% during sunny weather conditions, the same reliability can only be achieved for the



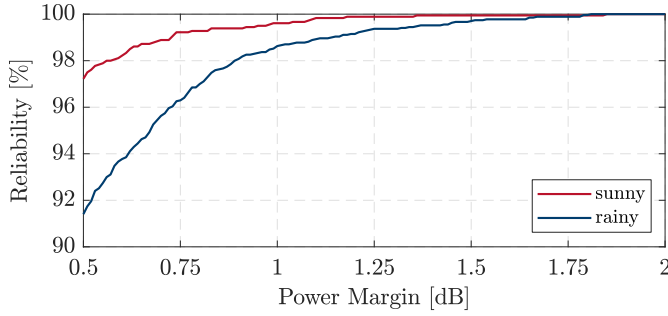


Fig. 4. Impact of power margin on the FSO channel reliability, as per definition of expression (3), under sunny and rainy weather conditions. Power estimation is performed by a moving average with optimized number of taps.

rainy weather scenario by increasing this power margin to more than 1.8 dB. Therefore, besides the inevitable capacity reduction due to the lower average received optical power (about 0.8 dB extra loss), the additional required margin (about 0.5 dB) for reliable communication will further penalize the overall capacity of the FSO system during rainy conditions.

It is important to stress out that these power margin values already consider the use of the proposed real-time power estimator. Instead, if no power budget monitoring is performed on the FSO system, then the required power margins must be increased, as it can be directly inferred from the instantaneous power measurements in Fig. 2.

Despite the high degree of reliability provided by the optimization of the operating power margin, as shown in Fig. 4, it must be referred that the impact of sporadic deep fades might threaten the very tight requirements for ultra-reliable 5G-compatible communications ( $\bar{R} > 99.999\%$ ). In addition, it should be referred that a stronger impact of atmospheric turbulence is expected in longer FSO links, in which case the probability of deep fades is increased. In those scenarios, exacerbating the optical power margin is not a viable solution, as it would heavily sacrifice the overall system capacity. Therefore, complementary reliability-enhancement techniques should be considered, such as the use of automatic repeat request protocols [40], [41] and spatial diversity FSO transmission schemes [42], [43].

#### D. Update-Rate Requirements for FSO Channel Monitoring

In order to ensure an accurate estimation of the received optical power, it is important to analyze the update-rate requirements for the moving average estimator of expression (1). To that purpose, we consider the rainy weather scenario, whose slow changes of precipitation rate yield a long-enough coherence time, allowing its analysis with the considered optical power sampling-rate. Starting from the nominal sampling-rate of the utilized power meter (0.25 Hz, i.e. a sampling period of 4 s), we digitally downsample the registered optical power measurements in order to analyze its impact on the NRMSE of the FSO channel estimation. The obtained results for the rainy weather scenario are depicted in Fig. 5, in which we also consider the joint optimization of the memory depth of the moving average channel estimator.

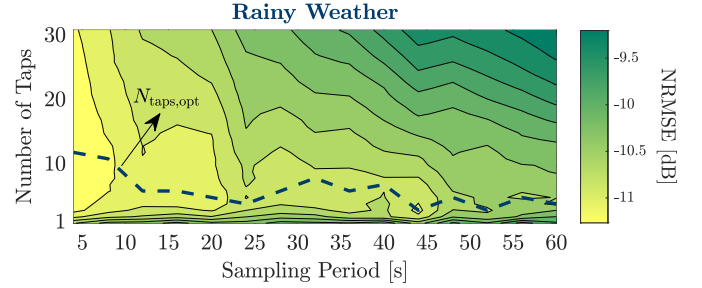


Fig. 5. Joint impact of update-rate and memory depth of the moving average estimator on the NRMSE of the received optical power estimation.

As expected, it becomes clear that increasing the sampling period between optical power measurements (i.e. decreasing the update-rate of the estimator) requires to reduce the total number of taps, so that a similar time-domain memory is kept. Nevertheless, even considering rather long sampling periods of about 20–30 s, we can observe that the NRMSE degradation is almost negligible. It is also worth noting that the corresponding optimum memory depth in that case is reduced to the range of 3 to 5 taps.

### III. ADAPTIVE PROBABILISTIC SHAPED MODULATION

The channel estimation tools proposed and demonstrated in the previous section can be utilized to optimize the capacity and reliability of outdoor FSO transmission systems. An effective way of achieving this goal is through the adaptation of the transmitted bit-rate to the time-varying SNR of the link<sup>1</sup>. Although a plethora of feasible options can be considered to that end, in this paper we shall consider the specific case of single-carrier coherent optical communications, owing to its progressive adoption and envisaged predominance in short-reach optical links. In that regard, the recently proposed and commercially deployed PCS modulation provides an attractive solution for highly flexible and granular bit-rate adaptation.

In the following we will review the basics of PCS format design, focusing on its potential for adaptive bit-rate provisioning in transmission systems with time-varying SNR conditions. For further details on PCS implementation aspects, the reader may refer to the literature [53], [54].

#### A. The PAS Architecture and Achievable Bit-Rates

The general concept of PCS modulation resorting to the reverse concatenation principle associated with the probabilistic amplitude shaping (PAS) scheme is illustrated in Fig. 6. The so-called *distribution matcher* is the key component of the PAS transmitter architecture, which is responsible for shaping the I and Q amplitude levels of the selected QAM template. This allows to allocate the remaining sign bits in the I and Q components (i.e. two bits in total) for carrying the systematic FEC parity bits, thus avoiding distorting the desired shaping through the FEC encoder. The

<sup>1</sup>Assuming the existence of fixed noise sources at the transmitter and receiver due to practical performance limitations (e.g. thermal and shot noise) then the variations on received optical power directly translate into proportional variations of SNR.

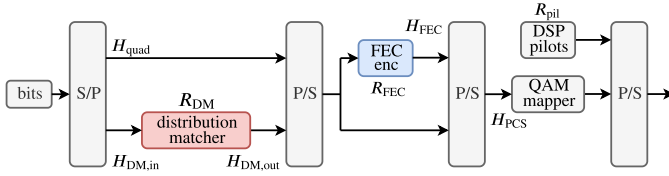


Fig. 6. PAS transmitter architecture with DSP pilots insertion. S/P: serial-to-parallel; P/S: parallel-to-serial.

total entropy that must be allocated for the FEC parity bits,  $H_{FEC}$ , can be calculated as,

$$H_{FEC} = (1 - R_{FEC}) \log_2(M_{PCS}), \quad (4)$$

where  $R_{FEC}$  is the FEC rate and  $M_{PCS}$  is the constellation size of the selected QAM template for PCS. Given the allocation of the FEC parity bits to the quadrant positions, the PAS scheme requires that  $H_{FEC} \leq 2$ , which consequently imposes that,

$$R_{FEC} \geq 1 - \frac{2}{\log_2(M_{PCS})}. \quad (5)$$

As an example, for a 64QAM template it results that  $R_{FEC} \geq 2/3$ . When the FEC rate is larger than the minimum imposed by expression (5), the remaining quadrant bits should be utilized to carry *unshaped* information bits. The available entropy for that effect is then simply given by,

$$H_{quad} = 2 - H_{FEC}. \quad (6)$$

Conversely, the information entropy fed to the distribution matcher,  $H_{DM,in}$ , is obtained from the amplitude bits in the QAM template,

$$H_{DM,in} = \log_2(M_{PCS}) - 2. \quad (7)$$

The distribution matcher will then provide fine control over its output entropy,

$$H_{DM,out} = H_{PCS} - 2, \quad (8)$$

where  $H_{PCS}$  is the overall desired PCS entropy given by,

$$H_{PCS} = \frac{R_b}{2R_s R_{pil}} + H_{FEC}, \quad (9)$$

where  $R_b$  is the target net bit-rate,  $R_s$  is the operating symbol-rate,  $R_{pil}$  is the digital signal processing (DSP) pilot-rate and the factor of two accounts for dual-polarization transmission.

Taking its input and output distribution entropies, the rate of the distribution matcher can simply be written as,

$$R_{DM} = \frac{H_{DM,out}}{H_{DM,in}}. \quad (10)$$

Considering the allocation of the information payload in the PAS scheme of Fig. 6, the overall net bit-rate of the transmitted PCS signal can be explicitly given by,

$$\begin{aligned} R_b &= 2R_s R_{pil} (H_{quad} + H_{DM,out}) = \\ &= 2R_s R_{pil} \left[ 2 - (1 - R_{FEC}) \log_2(M_{PCS}) \right. \\ &\quad \left. + R_{DM} (\log_2(M_{PCS}) - 2) \right], \end{aligned} \quad (11)$$

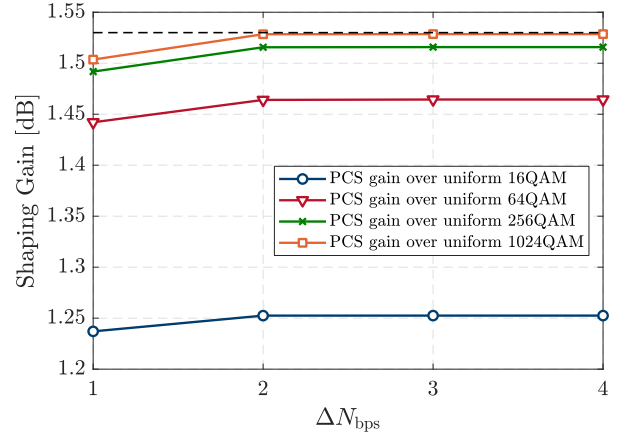


Fig. 7. Theoretically achievable shaping gain for uncoded modulation using the Maxwell-Boltzman symbol distribution of expression (14). The dashed line represents the theoretical maximum shaping gain of 1.53 dB.

where  $0 \leq R_{DM} \leq 1$  is the free parameter that can be adjusted in order to adapt the transmitted bit-rate. Given that the distribution matcher can only reduce the entropy of its input uniform distribution, i.e.  $R_{DM} \leq 1$ , it results that the maximum net bit-rate supported by the PAS transmitter architecture is,

$$R_{b,max} = 2R_s R_{FEC} R_{pil} \log_2(M_{PCS}). \quad (12)$$

The maximum bit-rate is then achieved for  $H_{PCS} = \log_2(M_{PCS})$ , i.e. for an uniform constellation, in which case the distribution matcher in Fig. 6 becomes a simple amplitude shift-keying (ASK) mapper for the I and Q components. Conversely, the minimum net bit-rate achievable by the PAS architecture is obtained when the distribution matcher collapses all its entries into a single output amplitude level, i.e.  $H_{DM,out} = 0$  and thus  $R_{DM} = 0$ . In that extreme case, a QPSK output constellation is obtained, yielding the following minimum net bit-rate,

$$R_{b,min} = R_{b,max} - 2R_s R_{pil} (\log_2(M_{PCS}) - 2), \quad (13)$$

where it is also implicit that the square QAM template for PCS must respect the condition  $M_{PCS} > 4$ .

### B. PCS Probability Distribution and Bit-Rate Adaptation

Besides enabling to adapt the transmitted net bit-rate, the distribution matcher can also be applied in favor of minimizing the average transmitted signal energy, thereby enhancing the energy efficiency of the transmission system. Following Shannon's theory for AWGN channels, the minimum transmitted signal energy required to achieve a given bit-rate is obtained by setting the QAM symbol probabilities,  $P_{x_n}$ , according to the Maxwell-Boltzman distribution [55],

$$P_{x_n} = \frac{\exp(-\lambda |x_n|^2)}{\sum_{n=1}^{M_{PCS}} \exp(-\lambda |x_n|^2)}, \quad (14)$$

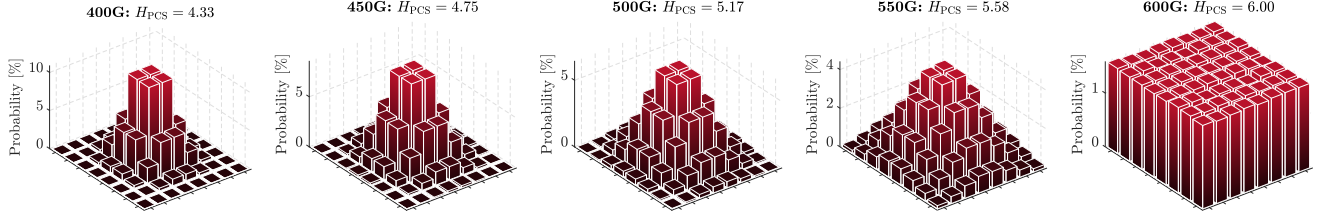


Fig. 8. Graphical illustration of the symbol probability distributions in a 64QAM PCS constellation for different bit-rates and considering  $R_s = 64$  Gbaud,  $M_{PCS} = 64$ ,  $R_{pil} = 15/16$  and  $R_{FEC} = 5/6$ .

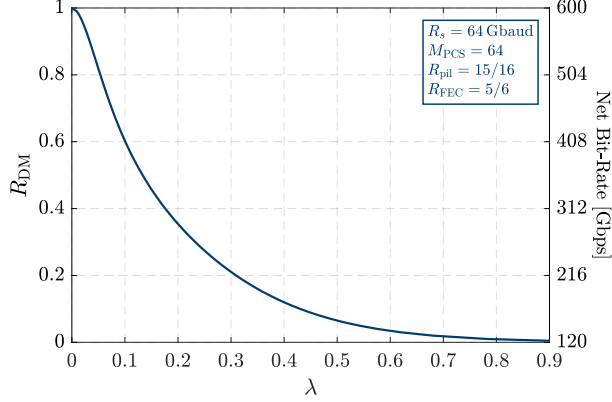


Fig. 9. Adapting the net bit-rate of PCS by tuning the shaping parameter,  $\lambda$ , associated with the Maxwell-Boltzman distribution. The considered signal parameters are  $R_s = 64$  Gbaud,  $M_{PCS} = 64$ ,  $R_{pil} = 15/16$  and  $R_{FEC} = 5/6$ .

where  $\lambda \geq 0$  is the shaping parameter and  $x_n$  is the  $n$ -th symbol in the square  $M_{PCS}$ -QAM constellation alphabet,

$$x_n = 2 \left( (n-1) \bmod \sqrt{M_{PCS}} \right) - \sqrt{M_{PCS}} + 1 + j \left( 2 \left\lceil \frac{n}{\sqrt{M_{PCS}}} \right\rceil - \sqrt{M_{PCS}} - 1 \right). \quad (15)$$

Note that a uniform distribution with symbol probabilities  $P_{x_n} = 1/M_{PCS}$  is obtained by setting  $\lambda = 0$ , which corresponds to  $R_{DM} = 1$ .

Considering the average energy of the corresponding constellations, we can evaluate the achievable shaping gain,  $G_{PCS}$ , provided by PCS using a QAM template of size  $M_{PCS}$  over a uniform QAM constellation of size  $M_{QAM}$  as,

$$G_{PCS} = 10 \log_{10} \left( \frac{\sum_n^{M_{QAM}} |u_n|^2}{\sum_k^{M_{PCS}} |s_k|^2 P_{s_k}} \right), \quad (16)$$

where  $u_n$  and  $s_n$  are the symbols of the uniform and shaped constellations, respectively, which are obtained by replacing the corresponding constellation sizes in expression (15). In [55] it has been demonstrated that the maximum shaping gain provided by PCS using the Maxwell-Boltzman distribution converges to 1.53 dB for large  $M_{QAM}$ . In order to verify this theoretical limit, in Fig. 7 we plot the value of  $G_{PCS}$  for different  $M_{QAM}$  and  $M_{PCS}$ , following expression (16), and optimizing the PCS probability distribution in order to yield the same net spectral efficiency as its uniform QAM counterpart. To simplify the analysis, we define  $M_{PCS} =$

$2^{\Delta N_{bps}} M_{QAM}$ . Two main conclusions can be extracted from the inspection of Fig. 7:

- As pointed out in [55], the shaping gain tends to asymptotically converge to the theoretical maximum of 1.53 dB (dashed line) as  $M_{QAM}$  is increased towards higher-order formats. The gap to the theoretical maximum is already less than 0.1 dB for a reference uniform 64QAM format;
- For a given reference uniform QAM constellation, the shaping gain achieved by PCS saturates for  $\Delta N_{bps} > 2$ , i.e. for  $M_{PCS} = 4M_{QAM}$ . As an example, this means that for a reference 16QAM uniform constellation, the maximum shaping gain of  $\sim 1.25$  dB can be achieved already with a 64QAM PCS constellation.

As an illustrative example of the PCS concept, let us consider the following particular case, which is matched with the experimental setup that will be presented in Section IV:

- $R_s = 64$  Gbaud;
- $M_{PCS} = 64$ ;
- $R_{pil} = 15/16$  (6.25% overhead for DSP pilots);
- $R_{FEC} = 5/6$  (20% overhead for FEC).

Utilizing expressions (12) and (13) with the aforementioned signal parameters, it results that the achievable net bit-rates with the PAS scheme are within the interval of 120 Gbps to 600 Gbps. Targeting a 400G+ implementation, a set of PCS constellation examples are shown in Fig. 8, corresponding to different bit-rates in the range of 400 Gbps to 600 Gbps. As previously exposed, the maximum bit-rate of 600 Gbps is obtained with an uniform 64QAM constellation, while lower bit-rates are achieved by adjusting the rate of the distribution matcher block in Fig. 6.

In practice, the adaptability of the transmitted net bit-rate shall be controlled by adjusting the shaping parameter,  $\lambda$ , in (14). Considering the previously enumerated set of signal parameters, the dependence of  $R_{DM}$  and  $R_b$  on  $\lambda$  is then shown in Fig. 9, which can be utilized as a look-up table (LUT) for setting  $\lambda$  according to the desired net bit-rate. Currently, there are several alternatives for a quasi-ideal practical implementation of the PCS distribution matcher, resorting to blockwise encoding of shaped bits and ensuring an invertible and fixed-length output [56], [60]–[62]. While the analysis of practical aspects of the distribution matcher implementation falls outside the scope of this work, for the remaining of this paper we shall adopt the constant composition distribution matcher (CCDM) algorithm proposed in [56].



### C. PCS Performance Assessment Metrics

In transmission systems utilizing the soft-decision (SD) FEC coding paradigm, it has been recently demonstrated that the generalized mutual information (GMI) is an adequate metric for pre-FEC performance assessment [63]. In an AWGN channel, and assuming a PCS-modulated transmitted signal, the GMI can be calculated as [64],

$$\text{GMI} = H_{\text{PCS}} - G(M_{\text{PCS}}, P_x, \sigma^2), \quad (17)$$

where  $G$  represents the loss of information due to propagation over the AWGN channel,

$$G(M_{\text{PCS}}, P_x, \sigma^2) = \frac{1}{N} \sum_{n=1}^N \sum_{k=1}^{\log_2(M_{\text{PCS}})} \log_2 \frac{\sum_{x_m \in \mathcal{X}} \exp\left(-\frac{|y_n - x_m|^2}{\sigma^2}\right) P_{x_m}}{\sum_{x_m \in \mathcal{X}(k, b_{n,k})} \exp\left(-\frac{|y_n - x_m|^2}{\sigma^2}\right) P_{x_m}}, \quad (18)$$

where  $\sigma^2$  is the noise variance of the AWGN channel,  $y_n$  is the  $n$ -th received symbol (out of a total of  $N$  symbols),  $x_m$  is the  $m$ -th symbol in the respective constellation alphabet,  $b_{n,k}$  is the  $k$ -th bit of the  $n$ -th transmitted symbol and  $\mathcal{X}(k, b)$  is a subset of the constellation alphabet,  $\mathcal{X}$ , which contains bit  $b \in [0, 1]$  in the  $k$ -th bit position. The GMI can then take values in the range of 0 to  $H_{\text{PCS}}$ , which ideally correspond to the worst and best SNR conditions, respectively. To provide an universal assessment of achievable information rate for any modulation format, the normalized GMI (NGMI) is commonly utilized, which can be defined as [65],

$$\text{NGMI} = 1 - \frac{G(M_{\text{PCS}}, P_x, \sigma^2)}{\log_2(M_{\text{PCS}})}. \quad (19)$$

Considering an ideal FEC implementation, it can be shown that the minimum NGMI that ensures error-free transmission,  $\text{NGMI}_{\text{th}}$ , is given by  $\text{NGMI}_{\text{th}} = R_{\text{FEC}}$ . However, due to practical implementation constraints, the SD-FEC encoder/decoder typically suffers from a coding gap, i.e. it imposes that  $\text{NGMI}_{\text{th}} = R_{\text{FEC}} + \delta$ , where  $\delta$  accounts for the non-ideal FEC performance loss.

Employing the NGMI definition of expression (19), in Fig. 10 we show the required SNR,  $\text{SNR}_{\text{req}}$ , as a function of the operating net bit-rate, considering the previously enumerated signal parameters and a realistic  $\text{NGMI}_{\text{th}} = 0.9$ , which is a typical value that guarantees post-FEC error-free transmission for most non-ideal SD-FEC algorithms [66] with 20% overhead ( $R_{\text{FEC}} = 5/6$ ). For direct comparison, we also show the required SNR associated with uniform 16QAM, 32QAM and 64QAM formats. The first key observation that can be taken from Fig. 10 is that the bit-rate adaptation through the sole modification of the modulation order provides a very coarse granularity of 100 Gbps for the considered scenario. In contrast, PCS provides a seamless and continuous bit-rate adaptation, requiring only to adjust the shaping parameter,  $\lambda$ , according to the desired bit-rate. This facilitates the real-time adaptation of the transmitted bit-rate to the time-varying SNR condition of the channel, provided that it can be accurately monitored. In addition, due to the minimization of

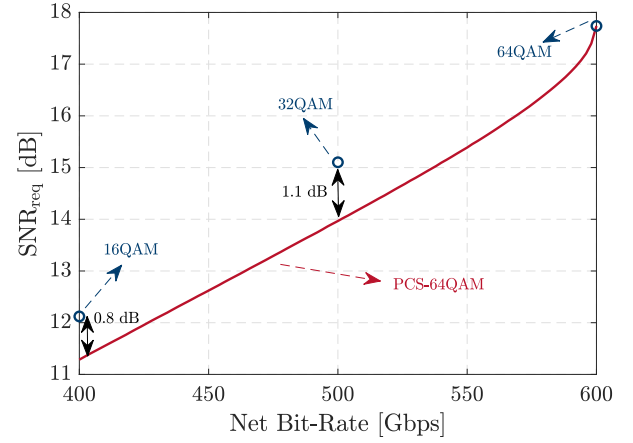


Fig. 10. Theoretically required SNR as a function of net bit-rate. The considered signal parameters are  $R_s = 64$  Gbaud,  $M_{\text{PCS}} = 64$ ,  $R_{\text{pil}} = 15/16$ ,  $R_{\text{FEC}} = 5/6$  and  $\text{NGMI}_{\text{th}} = 0.9$ .

the transmitted signal energy through the Maxwell-Boltzmann distribution, PCS also provides the well-known shaping gain over uniform modulation. For the considered scenario, this gain amounts to approximately 0.8 dB over uniform 16QAM and 1.1 dB over uniform cross-32QAM, for 400 Gbps and 500 Gbps transmission, respectively. The additional gain over 32QAM is mainly due to the imperfect Gray mapping associated with cross-QAM constellations, whose penalty is avoided by the square-QAM PCS constellation. Since a 64QAM template has been chosen for designing the PCS signal, the maximum supported bit-rate is 600 Gbps, in which case the transmitted signal becomes a uniform 64QAM constellation. In order to benefit from the PCS shaping gain, it can be seen from Fig. 10 that the transmitted bit-rate should not exceed 550 Gbps. Otherwise, a larger QAM template should be considered for designing the PCS signal.

### IV. TIME-ADAPTIVE 400G+ FSO TRANSMISSION

Taking advantage of the FSO channel estimation tools proposed in Section II and the PCS modulation concept reviewed in Section III, in this section we provide an integrated experimental demonstration of a time-adaptive 400G+ FSO transmission system, supported by long-term measurements. All experimental results presented in this section, as well as the corresponding post-processing routines, are available for consulting in an open access dataset [67].

#### A. Experimental Setup

The experimental setup utilized in this work is depicted in Fig. 11. After digital modulation, the baseband electrical signal is generated by an arbitrary waveform generator (AWG) operating at 120 Gsa/s (Keysight M8194A), with  $\sim 45$  GHz analog bandwidth. The PCS-64QAM signal is designed according to the methodology and parameters previously considered in Section III, rewritten here for clarity:  $R_s = 64$  Gbaud,  $M_{\text{PCS}} = 64$ ,  $R_{\text{pil}} = 15/16$ ,  $R_{\text{FEC}} = 5/6$  and  $\text{NGMI}_{\text{th}} = 0.9$ . Pulse shaping is performed with a root-raised cosine (RRC) filter with 0.05 roll-off factor. Optical

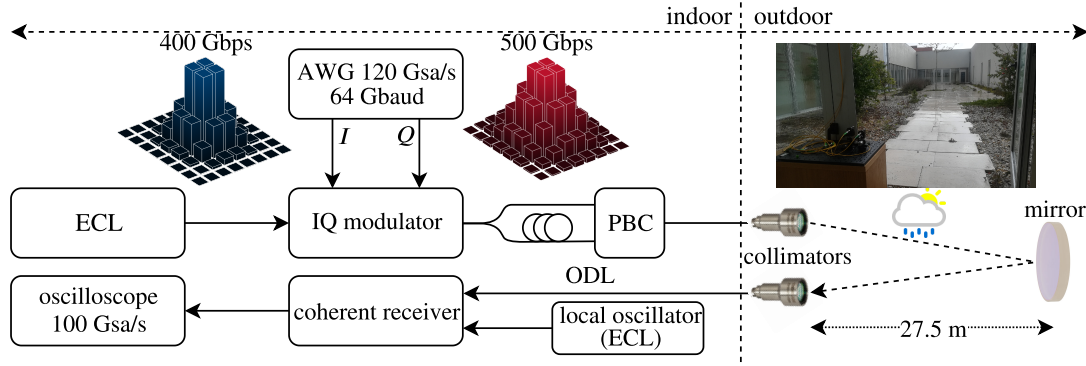


Fig. 11. Experimental setup for optical signal transmission and detection with a 55-m free-space optics link (inset in the upper right corner of the figure).

modulation is performed by a single-polarization IQ modulator with approximately 22 GHz bandwidth, which is fed by an external cavity laser (ECL) with 100 kHz nominal linewidth, emitting at 1550 nm with 15 dBm optical power. A 1 m optical delay line (ODL) is utilized to create a time-decorrelated copy of the IQ modulator output, which is then combined in the form of a dual-polarization signal by using a polarization-beam combiner (PBC). The dual-polarization optical signal is then sent to the 55 m FSO link, which follows the same configuration as the one previously described in Fig. 1. It is worth referring that the entire FSO link (fiber collimators and mirror) is fully exposed to the outdoor weather without any special protection. After transmission over the FSO link, a dual-polarization coherent receiver with  $\sim 40$  GHz bandwidth converts the optical signal back into the electrical domain. The local oscillator is also an ECL, whose parameters similar to the ones of the transmitter laser. The electrical I and Q components resulting from the coherent receiver are finally sampled and quantized by a 4-port real-time oscilloscope with 100 Gsa/s and 33 GHz analog bandwidth (Tektronix DPO70002SX).

Note that, in order to reduce the power consumption and cost of the system, no optical amplification is implemented either at the transmitter or at the receiver side. Therefore, the performance of the implemented transmission system will be mainly determined by the sensitivity of the coherent optical receiver, which sets the maximum power budget of the link.

### B. Digital Signal Processing Subsystems

The digital I and Q components of both polarizations captured from the real-time oscilloscope are processed in MATLAB, where a set of DSP subsystems is applied to compensate for the channel impairments and retrieve the transmitted signal information.

The first stages of DSP are aimed at compensating for the non-ideal characteristics of the receiver frontend, including IQ skew compensation and amplitude imbalance compensation resorting to the Gram-Schmidt orthogonalization algorithm [68]. Next, we perform polarization demultiplexing together with a first coarse channel equalization by applying the constant modulus algorithm (CMA) with 25 taps in a  $2 \times 2$  butterfly configuration. Carrier frequency offset estimation (around 200 MHz offset) and compensation are

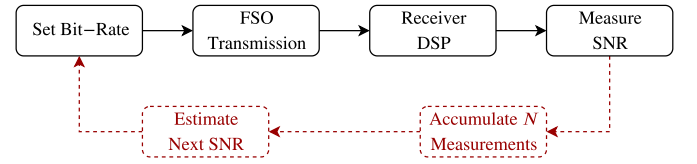


Fig. 12. Implemented methodology for the experimental validation of 400G+ adaptive FSO transmission.

then performed over the CMA-equalized signal, which is then followed by pilot-based carrier-phase recovery [69]. The inserted DSP pilots are QPSK-like symbols placed at the average energy of the original constellation, thereby avoiding any major impact on the shaping gain of the PCS signal. After carrier recovery, a second  $4 \times 4$  real-valued least-mean squares (LMS) adaptive equalizer with 51 taps is applied to fine-tune the equalization of the signal, also compensating for the residual transmitter-side IQ skew [70]. Convergence of both equalizers (CMA and LMS) is achieved through an initial data-aided training stage, followed by pilot-aided equalization. Finally, after downsampling and demapping, the NGMI is calculated according to expression (19). In order to directly estimate the SNR of the optical link, we also evaluate the error vector magnitude (EVM) between the fully-processed received signal and the transmitted one,

$$\text{EVM} = \sqrt{\frac{\sum_n |y(n) - x(n)|^2}{\sum_n |x(n)|^2}}. \quad (20)$$

Taking the EVM value obtained from expression (20), the SNR can be directly calculated as  $\text{SNR}_{\text{dB}} = -20 \log_{10}(\text{EVM})$ .

### C. FSO Channel Estimation and Bit-Rate Adaptation

The adopted methodology for bit-rate adaptation of the outdoor FSO transmission is depicted in the block diagram of Fig. 12. After FSO transmission and receiver-side DSP as described in the previous subsections, the measured SNR (from EVM) is fed to the moving average channel estimator introduced in Section II, thereby enabling to track and adapt to the time-varying power budget of the FSO link. In this

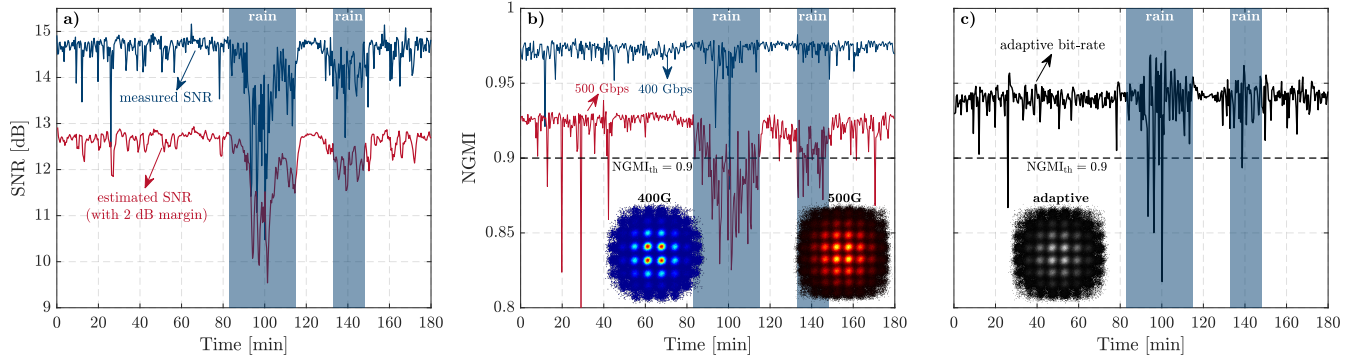


Fig. 13. (a) Measured SNR from the processed received signal and corresponding estimated SNR following the prediction rule (21); (b) obtained NGMI when the transmitted PCS-64QAM signal carries 400 Gbps and 500 Gbps; (c) obtained NGMI when adaptive PCS modulation is applied.

case, the power-based channel estimator of expression (1) is rewritten as,

$$SNR_{est}(n+1) = \frac{1}{\kappa N_{taps}} \sum_{n-N_{taps}+1}^n SNR_{meas}(n), \quad (21)$$

where  $SNR_{meas}(n)$  is the measured SNR (from EVM) and  $SNR_{est}(n+1)$  is the estimated SNR for the next time instant. In order to account for the variance of the FSO channel, a given SNR margin,  $\kappa$ , is also embedded in the estimation. Note that the power-based channel estimator of expression (1) could as well be considered for this experimental validation. However, the SNR-based tracking of expression (21) provides the advantage of enabling a fully-digital feedback, without the need for a dedicated optical power measurement.

Although the practical realization of the feedback system proposed in Fig. 12 is outside of the scope of this paper, several implementation options can be considered. In bidirectional FSO systems, a low overhead can be reserved in the reverse transmission direction in order to send the measured optical power back to the transmitter, which is then able to adapt its bit-rate accordingly. Considering typical bit-rates above 10 Gbps, the required overhead for this purpose would be negligible, even for significantly faster updates (e.g. once per millisecond). In addition, the processing and propagating latency of such point-to-point systems is typically much lower than this time-scale, and therefore, the feedback delay should not be significantly impacted by the transmission latency. An alternative solution for unidirectional FSO links (or other links in which the addition of an extra protocol overhead is not permitted), is the use of a parallel RF communication system, which among other possible functionalities, might be as well responsible for the implementation of the feedback channel. Depending on the update-rate requirements and available infrastructure, different technologies might be considered, such as cellular RF communications (4G, 5G), wireless fidelity or low-power IoT solutions (e.g. NB-IoT, LoRa, SigFox).

Due to the absence of a 400G+ real-time processing platform, each iteration of the bit-rate adaptation algorithm defined in Fig. 12 took an average of 25 seconds, already including the full processing of the adaptive modulation scheme. Taking this sampling period into account, and

considering the channel modeling results from Section II, we have defined  $N_{taps} = 3$  and  $\kappa = 1.585$  (2 dB) for the remaining of this work. We have then started a continuous measurement with the high-capacity transmission system depicted in Fig. 11, for a period of 3-hours. In each iteration, the oscilloscope obtains a batch of  $2 \times 10^5$  samples for 3 distinct modulation schemes using PCS-64QAM:

- i) fixed modulation at 400 Gbps ( $R_{DM} = 0.5833$ );
- ii) fixed modulation at 500 Gbps ( $R_{DM} = 0.7917$ );
- iii) adaptive modulation with the bit-rate adapted in accordance with the estimated SNR.

Taking the estimated SNR from expression (21), the estimated noise variance of the link can be simply evaluated as  $\sigma_{est}^2 = \sum_n |x(n)|^2 / SNR_{est}$ . Plugging the value of  $\sigma_{est}^2$  into expression (19), we can then numerically optimize the symbol probabilities in the PCS constellation,  $P_x$ , through the shaping parameter,  $\lambda$ , in expression (14), so that the NGMI converges to the pre-defined threshold of  $NGMI_{th} = 0.9$ . Note that, by tuning the  $\lambda$  parameter we are also implicitly modifying the rate of the distribution matcher,  $R_{DM}$ , as shown in Fig. 9, which consequently determines the transmitted bit-rate through expression (11). This concludes the bit-rate adaptation process implemented for case iii). In turn, since both the 400 Gbps and 500 Gbps configurations are fixed and do not depend on the SNR estimation, the data corresponding to cases i) and ii) is only stored in memory and processed afterwards, so that all measurements corresponding to cases i), ii) and iii) can be taken within a time lapse of 1-2 seconds, thus maximizing the time correlation between the three scenarios under comparison.

#### D. Experimental Results

Utilizing the experimental setup of Fig. 11 we have performed a 3-hours continuous measurement, whose results are depicted in Fig. 13. The outdoor measurements were taken during unstable meteorology, with the raining periods signaled by blue shaded areas. In Fig. 13a, we show the measured SNR (from the calculated EVM) and the respective estimated SNR (with 2 dB margin). In accordance with the modeling results previously presented in Section II, the impact of rain can be clearly identified by a significant reduction of the average

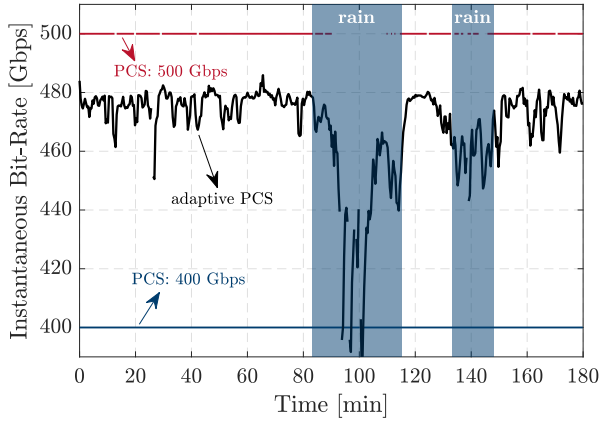


Fig. 14. Instantaneous transmitted bit-rate with fixed and adaptive modulation.

SNR of the channel. We can also confirm that the simple SNR estimator of expression (21) can accurately follow the trend of the time-varying FSO channel. The instantaneous performance of the FSO transmission system over time is measured in terms of NGMI of the processed signal. In this regard, Fig. 13b shows that the fixed 500G solution is significantly more affected during the raining periods, which is due to its higher required SNR: by operating farther from the NGMI saturation point, any small variation of SNR leads to a proportional variation of NGMI. This leads to several threshold NGMI violations, thereby bringing the system into out-of-service state for long periods of time. On the contrary, for the 400G case, the lower required SNR enables to operate significantly closer the NGMI saturation regime, in which case the experienced SNR variations in the link are partially absorbed by asymptotic convergence of expression (19) towards unity. This makes the 400G solution quite resilient to the worse channel conditions, due to its inherently large SNR margin for operation. However, this also means that the FSO channel is being heavily under-utilized for most of the time. In order to enable an improved utilization of the time-varying FSO channel capacity, in Fig. 13c we show the evolution of NGMI after adaptive entropy loading of the PCS constellation. Compared with the fixed 500G configuration, the adaptive bit-rate solution provides a more stable NGMI performance over the entire measurement period. Nevertheless, a higher performance variance is still observed during the raining periods, leading to a few violations of the NGMI threshold.

The instantaneous bit-rate evolution during the 3-hours measurement is presented in Fig. 14. Considering that the received signal cannot be correctly decoded when the NGMI is below the predefined target ( $\text{NGMI}_{\text{th}} = 0.9$ ), then the instantaneous bit-rate can be calculated as,

$$R_b(n) = \begin{cases} \text{eq. (11),} & \text{NGMI}(n) \geq \text{NGMI}_{\text{th}} \\ 0, & \text{otherwise.} \end{cases} \quad (22)$$

Note that the points corresponding to  $R_b(n) = 0$  are signaled in Fig. 14 by empty gaps on the corresponding bit-rate curves. In this sense, we can conclude that, although conservative, 400G transmission provides a resilient solution

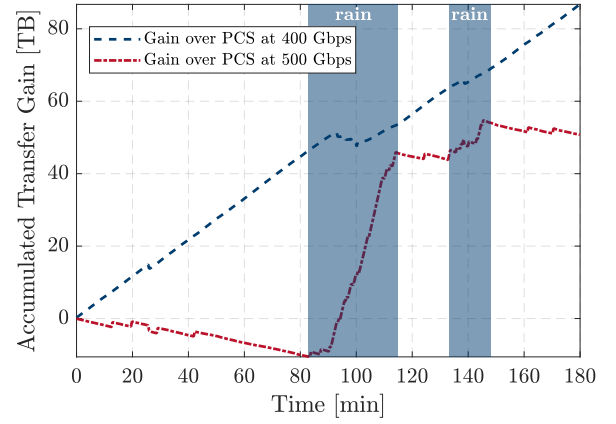


Fig. 15. Accumulated gain in data transfer (in Terabytes) over time obtained by time-adaptive modulation over fixed modulation.

for the FSO link under test, yielding an overall average bit-rate of 399.8 Gbps over the 3-hours measurement period. In contrast, the fixed 500G option corresponds to an optimistic estimation of the channel condition, enabling a very-high throughput during the best SNR periods, but failing catastrophically during the raining periods, thereby leading to an average bit-rate of 426.6 Gbps. In comparison with these fixed bit-rate scenarios, the adaptive PCS strategy effectively compensates for the worst channel condition with a reduction of transmitted bit-rate, thus relaxing the SNR requirements and thereby reducing the number of out-of-service occurrences. Consequently, an improved average bit-rate of 464 Gbps is achieved over the 3-hours measurement period.

Finally, in order to capture the overall picture in terms of bit-rate provisioning, in Fig. 15 we show the accumulated gain in data transfer achieved by the adaptive modulation scheme relatively to the fixed 400G and 500G strategies. Regarding the 400G signal, we can observe a steady increase of data transfer over time, except for a short interlude during the raining period, leading to an overall estimated gain of >80 Terabytes after the 3-hours measurement, i.e. an average bit-rate increase of about 64 Gbps. For the 500G signal instead, we can observe a slight penalty of the adaptive modulation during the first 80 minutes, which is due to the large considered SNR margin of 2 dB. Nevertheless, this initial loss is largely compensated by the rapid gain during the raining periods, leading to a total gain of >50 Terabytes after 3 hours, or conversely, ~37 Gbps increase in terms of average bit-rate.

## V. CONCLUSION

Free-space optical communications convey the potential for unparalleled wireless transmission capacity, enabled by electronic baseband processing together with commercial optical fiber transceivers. Through the use of simple passive components, such as optical fiber collimators, FSO can be made highly compatible with the already deployed optical fiber systems, thereby significantly reducing the cost and footprint for last-mile wireless access.

In this paper, we have tackled the modeling and mitigation of time-varying FSO channel impairments in outdoor weather-exposed links. Through the analysis of long-term power budget



measurements in a seamless fiber-FSO outdoor link, we have identified the existence of significant time correlation on the instantaneous SNR of outdoor FSO systems, which can be utilized to develop channel estimation techniques. This time-domain memory effect was found to strongly depend on the time-varying meteorology. In particular, it was found that under rainy weather the autocorrelation of the FSO channel can be on the order of several minutes, thereby enabling to employ low-frequency tracking techniques to capture the evolution of the average SNR on the channel. Using a simple and low-complexity algorithm based on an unweighted moving average, we have demonstrated the ability to accurately perform channel estimation on FSO links. Combining the proposed channel estimation technique with highly flexible modulation enabled by time-adaptive PCS, we have experimentally demonstrated a channel-aware blind bit-rate adaptation technique, enabling 400G+ transmission over 55 m during unstable atmospheric conditions. Future work comprises the extension of the proposed adaptive modulation technique to track and compensate for faster optical power variations generated by atmospheric turbulence, by integrating the feedback mechanism in a real-time processing platform, with a fast enough update rate.

## REFERENCES

- [1] Ericsson, "Ericsson mobility report," Tech. Rep., 2019.
- [2] *Technical Specification Group Services and System Aspects: Release 15 Description*, 3GPP TR 21.915.
- [3] S. Rangan, T. S. Rappaport, and E. Erkip, "Millimeter-wave cellular wireless networks: Potentials and challenges," *Proceedings of the IEEE*, vol. 102, no. 3, pp. 366–385, Mar. 2014.
- [4] K. David and H. Berndt, "6G vision and requirements: Is there any need for beyond 5G?" *IEEE Vehicular Technology Magazine*, vol. 13, no. 3, pp. 72–80, Sep. 2018.
- [5] T. Kawanishi, "THz and photonic seamless communications," *Journal of Lightwave Technology*, vol. 37, no. 7, pp. 1671–1679, Feb. 2019.
- [6] C. Wang, J. Yu, X. Li, P. Gou, and W. Zhou, "Fiber-THz-fiber link for THz signal transmission," *IEEE Photonics Journal*, vol. 10, no. 2, pp. 1–6, Apr. 2018.
- [7] K. Liu, S. Jia, S. Wang, X. Pang, W. Li, S. Zheng, H. Chi, X. Jin, X. Zhang, and X. Yu, "100 Gbit/s THz photonic wireless transmission in the 350-GHz band with extended reach," *IEEE Photonics Technology Letters*, vol. 30, no. 11, pp. 1064–1067, Jun. 2018.
- [8] S. Jia, X. Pang, O. Ozolins, X. Yu, H. Hu, J. Yu, P. Guan, F. Da Ros, S. Popov, G. Jacobsen, M. Galili, T. Morioka, D. Zibar, and L. K. Oxenløwe, "0.4 THz photonic-wireless link with 106 Gb/s single channel bitrate," *Journal of Lightwave Technology*, vol. 36, no. 2, pp. 610–616, Jan. 2018.
- [9] I. Dan, G. Ducournau, S. Hisatake, P. Szriftgiser, R. Braun, and I. Kallfass, "A terahertz wireless communication link using a superheterodyne approach," *IEEE Transactions on Terahertz Science and Technology*, vol. 10, no. 1, pp. 32–43, Jan. 2020.
- [10] T. Nagatsuma, K. Oogimoto, Y. Yasuda, Y. Fujita, Y. Inubushi, S. Hisatake, A. M. Agoues, and G. C. Lopez, "300-GHz-band wireless transmission at 50 Gbit/s over 100 meters," in *Proc. and Terahertz waves (IRMMW-THz) 2016 41st Int. Conf. Infrared, Millimeter*, Sep. 2016.
- [11] T. Harter, C. Füllner, J. N. Kemal, S. Ummethala, M. Brosi, E. Bründermann, W. Freude, S. Randel, and C. Koos, "110-m THz wireless transmission at 100 Gbit/s using a Kramers-Kronig Schottky barrier diode receiver," in *Proc. European Conf. Optical Communication (ECOC)*, Sep. 2018.
- [12] A. S. Hamza, J. S. Deogun, and D. R. Alexander, "Classification framework for free space optical communication links and systems," *IEEE Communications Surveys Tutorials*, vol. 21, no. 2, pp. 1346–1382, 2019.
- [13] I. Alimi, A. Shahpari, A. Sousa, R. Ferreira, P. Monteiro, and A. Teixeira, "Challenges and opportunities of optical wireless communication technologies," in *Optical Communication Technology*, P. Pinho, Ed. Rijeka: InTech, 2017, ch. 02.
- [14] M. A. Khalighi and M. Uysal, "Survey on free space optical communication: A communication theory perspective," *IEEE Communications Surveys Tutorials*, vol. 16, no. 4, pp. 2231–2258, 2014.
- [15] P. Wilke Berenguer, D. Schulz, J. Hilt, P. Hellwig, G. Kleinpeter, J. K. Fischer, and V. Jungnickel, "Optical wireless MIMO experiments in an industrial environment," *IEEE Journal on Selected Areas in Communications*, vol. 36, no. 1, pp. 185–193, Jan. 2018.
- [16] H. Kaushal and G. Kaddoum, "Optical communication in space: Challenges and mitigation techniques," *IEEE Communications Surveys Tutorials*, vol. 19, no. 1, pp. 57–96, 2017.
- [17] A. N. Sousa, I. A. Alimi, R. M. Ferreira, A. Shahpari, M. Lima, P. P. Monteiro, and A. L. Teixeira, "Real-time dual-polarization transmission based on hybrid optical wireless communications," *Optical Fiber Technology*, vol. 40, pp. 114 – 117, Jan. 2018.
- [18] A. Lorences-Riesgo, F. P. Guiomar, A. N. Sousa, A. L. Teixeira, N. J. Muga, M. C. R. Medeiros, and P. P. Monteiro, "200 G outdoor free-space-optics link using a single-photodiode receiver," *Journal of Lightwave Technology*, vol. 38, no. 2, pp. 394–400, Jan. 2020.
- [19] M. Alzenad, M. Z. Shakir, H. Yanikomeroglu, and M. S. Alouini, "FSO-based vertical backhaul/fronthaul framework for 5G+ wireless networks," *IEEE Communications Magazine*, vol. 56, no. 1, pp. 218–224, Jan. 2018.
- [20] A. O. Mufutau, F. P. Guiomar, M. A. Fernandes, A. Lorences-Riesgo, A. Oliveira, and P. P. Monteiro, "Demonstration of a hybrid optical fiber–wireless 5G fronthaul coexisting with end-to-end 4G networks," *J. Opt. Commun. Netw.*, vol. 12, no. 3, pp. 72–78, Mar. 2020.
- [21] P. T. Dat, A. Bekkali, K. Kazaura, K. Wakamori, and M. Matsumoto, "A universal platform for ubiquitous wireless communications using radio over FSO system," vol. 28, pp. 2258–2267, 2010.
- [22] A. Vavoulas, H. G. Sandalidis, and D. Varoutas, "Weather effects on FSO network connectivity," *IEEE/OSA Journal of Optical Communications and Networking*, vol. 4, no. 10, pp. 734–740, Oct. 2012.
- [23] M. Z. Hassan, M. J. Hossain, J. Cheng, and V. C. M. Leung, "Effective capacity of coherent POLMUX OWC impaired by atmospheric turbulence and pointing errors," *J. Lightwave Technol.*, vol. 34, no. 21, pp. 5007–5022, Nov. 2016.
- [24] L. C. Andrews, R. L. Phillips, C. Y. Hopen, and M. A. Al-Habash, "Theory of optical scintillation," *J. Opt. Soc. Am. A*, vol. 16, no. 6, pp. 1417–1429, Jun. 1999.
- [25] J. H. Churnside and S. F. Clifford, "Log-normal rician probability-density function of optical scintillations in the turbulent atmosphere," *J. Opt. Soc. Am. A*, vol. 4, no. 10, pp. 1923–1930, Oct. 1987.
- [26] A. Al-Habash, L. C. Andrews, and R. L. Phillips, "Mathematical model for the irradiance probability density function of a laser beam propagating through turbulent media," *Optical Engineering*, vol. 40, no. 8, pp. 1554 – 1562, Aug. 2001.
- [27] A. Ishimaru, "Theory and application of wave propagation and scattering in random media," *Proceedings of the IEEE*, vol. 65, no. 7, pp. 1030–1061, Jul. 1977.
- [28] A. Mostafa and S. Hranilovic, "Channel measurement and Markov modeling of an urban free-space optical link," *IEEE/OSA Journal of Optical Communications and Networking*, vol. 4, no. 10, pp. 836–846, Oct. 2012.
- [29] S. T. Hong and A. Ishimaru, "Two-frequency mutual coherence function, coherence bandwidth, and coherence time of millimeter and optical waves in rain, fog, and turbulence," *Radio Science*, vol. 11, no. 6, pp. 551–559, 1976.
- [30] C. H. Liu and K. C. Yeh, "Propagation of pulsed beam waves through turbulence, cloud, rain, or fog," *J. Opt. Soc. Am.*, vol. 67, no. 9, pp. 1261–1266, Sep. 1977.
- [31] H. Lu, W. Zhao, and X. Xie, "Analysis of temporal broadening of optical pulses by atmospheric dispersion in laser communication system," *Optics Communications*, vol. 285, no. 13, pp. 3169 – 3173, Jun. 2012.
- [32] R. S. Lawrence and J. W. Strohbehn, "A survey of clear-air propagation effects relevant to optical communications," *Proceedings of the IEEE*, vol. 58, no. 10, pp. 1523–1545, Oct. 1970.
- [33] F. Xu, A. Khalighi, P. Caussé, and S. Bourennane, "Channel coding and time-diversity for optical wireless links," *Opt. Express*, vol. 17, no. 2, pp. 872–887, Jan. 2009.
- [34] O. Barsimantov and V. Nikulin, "Adaptive optimization of a free space laser communication system under dynamic link attenuation," *IEEE/OSA Journal of Optical Communications and Networking*, vol. 3, no. 3, pp. 215–222, Mar. 2011.



- [35] M. Karimi and M. Uysal, "Novel adaptive transmission algorithms for free-space optical links," *IEEE Transactions on Communications*, vol. 60, no. 12, pp. 3808–3815, Dec. 2012.
- [36] I. B. Djordjevic and G. T. Djordjevic, "On the communication over strong atmospheric turbulence channels by adaptive modulation and coding," *Opt. Express*, vol. 17, no. 20, pp. 18 250–18 262, Sep. 2009.
- [37] I. B. Djordjevic, "Adaptive modulation and coding for free-space optical channels," *IEEE/OSA Journal of Optical Communications and Networking*, vol. 2, no. 5, pp. 221–229, May 2010.
- [38] H. Safi, A. A. Sharifi, M. T. Dabiri, I. S. Ansari, and J. Cheng, "Adaptive channel coding and power control for practical fso communication systems under channel estimation error," *IEEE Transactions on Vehicular Technology*, vol. 68, no. 8, pp. 7566–7577, Aug. 2019.
- [39] J. A. Anguita, M. A. Neifeld, B. Hildner, and B. Vasic, "Rateless coding on experimental temporally correlated fso channels," *Journal of Lightwave Technology*, vol. 28, no. 7, pp. 990–1002, Apr. 2010.
- [40] K. Kiasaleh, "Hybrid ARQ for fso communications through turbulent atmosphere," *IEEE Communications Letters*, vol. 14, no. 9, pp. 866–868, Sep. 2010.
- [41] S. M. Aghajanzadeh and M. Uysal, "Information theoretic analysis of hybrid-ARQ protocols in coherent free-space optical systems," *IEEE Transactions on Communications*, vol. 60, no. 5, pp. 1432–1442, May 2012.
- [42] A. Jaiswal, M. R. Bhatnagar, P. Soni, and V. K. Jain, "Differential optical spatial modulation over atmospheric turbulence," *IEEE Journal of Selected Topics in Signal Processing*, vol. 13, no. 6, pp. 1417–1432, Oct. 2019.
- [43] A. S. Ghazy, M. A. Hasabelnaby, H. A. I. Selmy, and H. M. H. Shalaby, "Optimal transceiver placement and resource allocation schemes in cooperative dynamic fso networks," *J. Opt. Commun. Netw.*, vol. 11, no. 11, pp. 512–524, Nov. 2019.
- [44] L. Mroueh, "Extended golden light code for fso-MIMO communications with time diversity," *IEEE Transactions on Communications*, vol. 67, no. 1, pp. 553–563, Jan. 2019.
- [45] and Xiaoming Zhu and J. M. Kahn, "Free-space optical communication through atmospheric turbulence channels," *IEEE Transactions on Communications*, vol. 50, no. 8, pp. 1293–1300, Aug. 2002.
- [46] —, "Markov chain model in maximum-likelihood sequence detection for free-space optical communication through atmospheric turbulence channels," *IEEE Transactions on Communications*, vol. 51, no. 3, pp. 509–516, Mar. 2003.
- [47] W. Zhang, S. Hranilovic, and C. Shi, "Soft-switching hybrid fso/RF links using short-length raptor codes: Design and implementation," *IEEE Journal on Selected Areas in Communications*, vol. 27, no. 9, pp. 1698–1708, Dec. 2009.
- [48] A. Abdulhussein, A. Oka, T. T. Nguyen, and L. Lampe, "Rateless coding for hybrid free-space optical and radio-frequency communication," *IEEE Transactions on Wireless Communications*, vol. 9, no. 3, pp. 907–913, Mar. 2010.
- [49] M. Lu, L. Liu, and S. Hranilovic, "Raptor-coded free-space optical communications experiment," *IEEE/OSA Journal of Optical Communications and Networking*, vol. 8, no. 6, pp. 398–407, Jun. 2016.
- [50] A. G. Alkholidi and K. S. Altowij, "Free space optical communications — theory and practices," in *Contemporary Issues in Wireless Communications*. InTech, 2014.
- [51] G. Bosco, "Advanced modulation techniques for flexible optical transceivers: The rate/reach tradeoff," vol. 37, pp. 36–49, Jan. 2019.
- [52] F. Buchali, F. Steiner, G. Böcherer, L. Schmalen, P. Schulte, and W. Idler, "Rate adaptation and reach increase by probabilistically shaped 64-QAM: An experimental demonstration," *J. Lightw. Technol.*, vol. 34, no. 7, pp. 1599–1609, Apr. 2016.
- [53] G. Böcherer, P. Schulte, and F. Steiner, "Probabilistic shaping and forward error correction for fiber-optic communication systems," *Journal of Lightwave Technology*, vol. 37, no. 2, pp. 230–244, Jan. 2019.
- [54] J. Cho and P. J. Winzer, "Probabilistic constellation shaping for optical fiber communications," *Journal of Lightwave Technology*, vol. 37, no. 6, pp. 1590–1607, Mar. 2019.
- [55] F. R. Kschischang and S. Pasupathy, "Optimal nonuniform signaling for Gaussian channels," *IEEE Trans. Inf. Theory*, vol. 39, no. 3, pp. 913–929, May 1993.
- [56] P. Schulte and G. Böcherer, "Constant composition distribution matching," *IEEE Trans. Inf. Theory*, vol. 62, no. 1, pp. 430–434, Jan. 2016.
- [57] F. P. Guiomar, L. Bertignono, D. Pileri, A. Nespola, G. Bosco, A. Carena, and F. Forghieri, "Comparing different options for flexible networking: Probabilistic shaping vs. hybrid subcarrier modulation," in *Proc. 43th European Conf. Optical Communication (ECOC)*, 2017, p. Th.1.E.3.
- [58] F. P. Guiomar, A. Lorences-Riesgo, D. Ranzal, F. Rocco, A. N. Sousa, A. Carena, A. L. Teixeira, M. C. R. Medeiros, and P. P. Monteiro, "High-capacity and rain-resilient free-space optics link enabled by time-adaptive probabilistic shaping," in *Proc. European Conf. Optical Communication (ECOC)*, Sep. 2019, p. Tu.3.C.3.
- [59] F. P. Guiomar, A. Lorences-Riesgo, D. Ranzal, F. Rocco, A. Carena, and P. P. Monteiro, "Experimental characterization of optical received power in an outdoor free-space optics link [data set]," *Zenodo*, 2020, <http://doi.org/10.5281/zenodo.3708496>.
- [60] T. Yoshida, M. Karlsson, and E. Agrell, "Hierarchical distribution matching for probabilistically shaped coded modulation," *Journal of Lightwave Technology*, vol. 37, no. 6, pp. 1579–1589, Mar. 2019.
- [61] T. Fehenberger, D. S. Millar, T. Koike-Akino, K. Kojima, and K. Parsons, "Multiset-partition distribution matching," *IEEE Transactions on Communications*, vol. 67, no. 3, pp. 1885–1893, Mar. 2019.
- [62] J. Cho and P. J. Winzer, "Multi-rate prefix-free code distribution matching," in *Proc. Optical Fiber Communications Conf. and Exhibition (OFC)*, Mar. 2019, p. M4B.7.
- [63] A. Alvarado, E. Agrell, D. Lavery, R. Maher, and P. Bayvel, "Replacing the soft-decision FEC limit paradigm in the design of optical communication systems," *Journal of Lightwave Technology*, vol. 33, no. 20, pp. 4338–4352, Oct. 2015.
- [64] A. Alvarado, T. Fehenberger, B. Chen, and F. M. J. Willems, "Achievable information rates for fiber optics: Applications and computations," *Journal of Lightwave Technology*, vol. 36, no. 2, pp. 424–439, Jan. 2018.
- [65] J. Cho, L. Schmalen, and P. J. Winzer, "Normalized generalized mutual information as a forward error correction threshold for probabilistically shaped QAM," in *Proc. European Conf. Optical Communication (ECOC)*, Sep. 2017.
- [66] J. Cho, S. L. I. Olsson, S. Chandrasekhar, and P. Winzer, "Information rate of probabilistically shaped QAM with non-ideal forward error correction," in *Proc. European Conf. Optical Communication (ECOC)*, Sep. 2018.
- [67] F. P. Guiomar, A. Lorences-Riesgo, D. Ranzal, F. Rocco, A. N. Sousa, M. A. Fernandes, B. T. Brandão, A. Carena, M. C. R. Medeiros, and P. P. Monteiro, "Free-space optics transmission with time-adaptive pcs modulation [data set]," *Zenodo*, 2019, <http://doi.org/10.5281/zenodo.3715346>.
- [68] I. Fatadin, S. J. Savory, and D. Ives, "Compensation of quadrature imbalance in an optical QPSK coherent receiver," *IEEE Photon. Technol. Lett.*, vol. 20, no. 20, pp. 1733–1735, Oct. 2008.
- [69] M. Magarini, L. Barletta, A. Spalvieri, F. Vacondio, T. Pfau, M. Pepe, M. Bertolini, and G. Gavioli, "Pilot-symbols-aided carrier-phase recovery for 100-G PM-QPSK digital coherent receivers," *IEEE Photon. Technol. Lett.*, vol. 24, no. 9, pp. 739–741, May 2012.
- [70] M. Faruk and K. Kikuchi, "Compensation for in-phase/quadrature imbalance in coherent-receiver front end for optical quadrature amplitude modulation," *IEEE Photonics Journal*, vol. 5, no. 2, pp. 7 800 110–7 800 110, Apr. 2013.